Chapter 11

Shock Compression of Porous Ceramics

Yin Yu and Hongliang He

Additional information is available at the end of the chapter

http://dx.doi.org/10.5772/intechopen.72246

Abstract

Shock compression is a challenge for porous ceramics in application. In this chapter, numerical simulation and experimental observation have been introduced, which reveals generation of crack, damage, and fracture within porous ceramics upon shock wave loading. Simulation of a two-dimensional lattice-spring model explains the effects of voids and grain boundaries on the mesoscopic deformation features of shocked porous ceramics. Experiments confirm the fracture and fragmentation evolution in the post-shock ceramics. These understandings are conducive to the design, manufacture and usage of the porous ceramics under rapid impulsive loading. Furthermore, the concept of controllable fracture is proposed, which is a strategy to modulate the propagation of shock fracture in porous ceramics for the avoidance or delay of the shock-induced functional failure. It is evidenced that a "shielded region," i.e., free of severe shock fracture, could be formed with the sacrifice of a "damaged region" in the porous ceramics.

Keywords: porous ceramics, shock compression, lattice-spring model, deformation mechanisms, damage shielding

1. Introduction

Shock wave loading is generated often at impact, collision, and blast. A shock wave is a powerful amplifier of defects in that it activates pre-existing defects (e.g., microvoids, cracks, and grain boundaries), extends cracks, and breaks media. The main challenge of porous ceramics in the application upon shock wave loading is its nonstationary behavior due to crack, damage, and fracture of the heterogeneous structure [1–4]. Mechanical, electrical, and optical properties of ceramics are severely affected by shock waves, and consequently, it may deteriorate the designed functions of shocked ceramics, such as in the cases of high-strength ceramics for armor [5], piezoelectric and ferroelectric ceramics for converting mechanical energy to electrical energy [6–8] and transparent ceramics for optical measurements in shock experiments [9].

Hence, a good understanding of the dynamic response of porous ceramics under rapid impulsive loading is vital to the design, manufacture, and usage of these materials. To this objective, a two-dimensional lattice-spring model (LSM) has been newly established, and the shock compression behavior of porous ceramics is explored and the mechanisms and strategies for improving robustness are discussed.

2. Model of porous ceramics under shock wave compression

Dynamic response of porous ceramics under rapid impulsive loading relates to evolution of a crack network following the shock wave. Although some pioneer works have been conducted on modeling ceramic shock fracture via mesh-based computational methods [10–13], such methods encounter significant difficulties when dealing with fracture and fragmentation induced by shock wave compression. The reason is that partial derivatives are used in mesh-based methods to represent the relative displacement and force between any two neighboring particles [14]. But, the necessary partial derivatives with respect to the spatial coordinates are undefined along the cracks and need to be redefined. However, the redefinition requires us to know where the discontinuity is located. This limits the usefulness of these methods in addressing problems involving the spontaneous formation of cracks, in which one might not know their location in advance [14]. In contrast, as a particle method, the lattice-spring model (LSM, also known as discrete-element method) [15–20] could avoid various numerical difficulties caused by displacement discontinuity. In this section, details of the LSM model (lattice interactions, spring mapping procedure, fracture criterion, microstructures, loading) and its validation are introduced.

2.1. Lattice-spring model

A two-dimensional LSM was established to explore the shock behavior of porous ceramics. In the LSM, continuum medium is described as discrete material particles. The nearest neighboring particles are interconnected and interact through springs. Evolution of this network can represent the global response of macroscopic materials, if the interactions of material particles are described accurately. Through simplifications of real materials and the model's discrete nature, LSM has the advantage in treating fracture, fragmentation, and other dynamic damage processes of brittle materials subjected to tension, compression, shear, and other complex loading [17].

The model established here has an elastic-brittle interaction, which ignores the small plasticity contribution to the response that possibly exists in brittle materials; only a linear elastic interaction is used. Particle interaction is shown in **Figure 1**. Between pairs of nearest-neighbor particles, indexed by i and j, there are the central potential forces f_{ij}^{n} and the shear resistance forces f_{ij}^{τ}. They could be visualized as forces provided by a normal spring that lies along the normal direction and a shear spring that lies along the tangent direction.

An energy threshold based on Griffith's energy balance principle [21] has been used as the fracture criterion. The summation of the deformation energy induced by tension in the normal spring and shear in the shear spring is calculated when the relative position between two neighboring particles changes. And the two springs break irreversibly to create a microcrack between the two

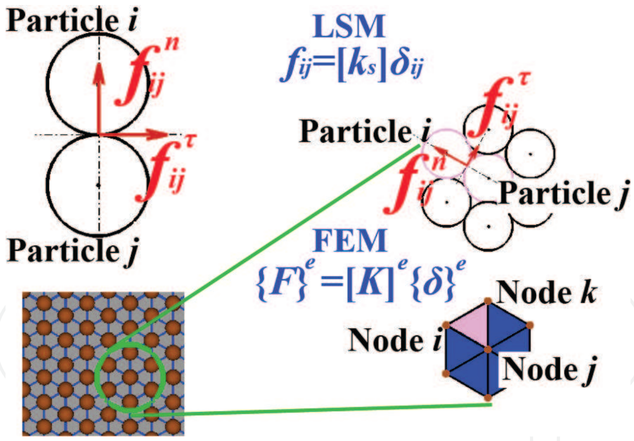

Figure 1. Particle interaction in the LSM model and schematic of the parameter mapping procedure.

particles, when the sum exceeds a certain threshold corresponding to the fracture energy. The deformation energy induced by compression in the normal spring will not be counted in this criterion, because it is assumed that hydrostatic compression would not cause fracture in the homogeneous media. When the microcrack forms between two particles, tension and shear interactions are removed; however, repulsion and friction interactions exist, when the broken particles come into collision.

2.2. Parameter mapping procedure

The parameters used in the interaction formulae of LSM were usually given empirically, resulting in a qualitative representation of mechanical properties of target materials. Several outstanding studies have been done to overcome this shortcoming [14–16, 22–25]. Gusev proposed a parameter mapping procedure between finite-element method (FEM) and LSM [26]: consider a network that is both a LSM lattice and a FEM mesh; first, elastic constants of the target material are transformed into stiffness matrix of the FEM mesh; next, using the same network, the interaction-parameter conversion between FEM and LSM is performed (**Figure 1**).

To obtain the deformation state for the FEM mesh, the force-displacement equations assembled from all elements need to be solved, that is,

$$\{F\} = [K]\{\delta\} \tag{1}$$

where $\{F\}$ and $\{\delta\}$ are the respective column vectors formed from the external forces and displacements of all nodes. The so-called global stiffness matrix $[K]$ is a sparse symmetric matrix, which is determined by elastic constants of the material and geometrical structure of the mesh. Under the equilibrium state, the internal force f_i acting on node i can be written, according to Eq. (1), as

$$f_i = -F_i = -\left(K_{i1}\times\delta_1 + K_{i2}\times\delta_2 + \cdots + K_{ii}\times\delta_i + \cdots + K_{ij}\times\delta_j + \cdots + K_{iN}\times\delta_N\right) \tag{2}$$

Since motion of translation would not change the strain energy of the whole system, Eq. (3) holds between elements of the matrix $[K]$ [26],

$$K_{ii} = -\sum_{\substack{x=1 \\ x\neq i}}^{N} K_{ix} \tag{3}$$

Using K_{ii}, Eq. (3) could be rearranged as

$$\begin{aligned} f_i &= -\left[K_{i1} \times \delta_1 + K_{i2} \times \delta_2 + \cdots + \left(-\sum_{\substack{x=1 \\ x\neq i}}^{N} K_{ix} \times \delta_i\right) + \cdots + K_{ij} \times \delta_j + \cdots + K_{iN} \times \delta_N\right] \\ &= -\left\{\left[K_{i1} \times (\delta_1 - \delta_i)\right] + \left[K_{i2}(\delta_2 - \delta_i)\right] + \left[K_{ij}(\delta_j - \delta_i)\right] + \left[K_{iN}(\delta_N - \delta_i)\right]\right\} \\ &= \sum_{\substack{x=1 \\ x\neq i}}^{N} K_{ix}(\delta_i - \delta_x) = \sum_{\substack{x=1 \\ x\neq i}}^{N} f_{ix} \end{aligned} \tag{4}$$

The resultant internal force f_i is the sum of the forces from all the neighbor particles (1, 2,…, j,…, N; i excluded). Hence, the internal force acting on particle i by particle j is

$$f_{ij} = K_{ij}\left(\delta_i - \delta_j\right) = K_{ij}\delta_{ij} \tag{5}$$

where $\delta_{ij} = \delta_i - \delta_j$. Eq. (5) has the form of Hooke's law. The K_{ij} could be taken as the stiffness coefficients of the springs of the LSM.

2.3. Model validation

In order to validate the parameter mapping procedure, dense and porous samples have been built and tested. Young's modulus, E_0 = 250 GPa; shear modulus, G_0 = 104 GPa; and density $\rho = 5 \times 10^3$ kg/m^3 are set into the lattice-spring networks of those samples. Samples with porosity 0, 2, 4, 6, 8, and 10% are subjected to quasi-static compression and tension. The maximum and minimum strains are 0.1 and −0.1%, respectively. Young's modulus of the dense sample is 251 GPa, which is in good agreement with the preset E_0 [17]. In porous samples, Young's modulus decreases with the porosity increasing.

Shear wave speeds (C_s) of dense and porous samples have been obtained via acoustic velocity tests. Then, the shear modulus $G = \rho C_s^2$ could be calculated. For the dense sample, shear modulus is 105 GPa, which is almost the same with the preset G_0 [17]. As the porosity increases, shear modulus decreases. In rock physics, the elastic property of rock with spherical pores could be estimated from [27]

$$\beta_{eff}(\eta) = \beta_s\left(1 + \frac{3(1 - v_s)}{2(1 - 2\,v_s)}\frac{\eta}{1 - \eta}\right) \tag{6}$$

where β_s is the compression coefficient (the inverse of bulk modulus) of the dense medium, β_{eff} the effective compression coefficient of the porous medium, v_s Poisson's ratio of the dense medium, and η porosity. With

$$G(\eta) = \frac{3E(\eta)}{\left(9 - \beta_{eff}(\eta)E(\eta)\right)} \tag{7}$$

together with $\beta_{eff}(\eta)$ estimated from Eq. (6) and Young's moduli $E(\eta)$ obtained from the simulation, the shear moduli $G(\eta)$ of the porous samples could be worked out. G/G_0 extracted directly from acoustic velocity tests are in good agreement with G/G_0 estimated via Eq. (7) [17]. Thus, the parameter-mapping procedure is verified as having the capability of representing elastic properties of both dense and porous brittle medium quantitatively.

2.4. Microstructures and shock wave loading

To capture the influence of grain boundaries (GBs) on porous ceramics, polycrystalline sketching has been randomly produced using Voronoi tessellation [10]. As shown in **Figure 2(a)**, particles (small circles) in the model are assigned into grains (large polygons). If two particles connected by springs belong to different grains, then the springs are assumed to be a small segment of a GB. Given that media on GBs have higher energy state than media in grains, the deformation energy required for creating a pair of new crack surfaces on GBs is smaller than that in grains. The energy threshold on GBs is given as $U_S^{GB} = U_S^{grain} - E^{GB}$, where U_S^{grain} and E^{GB} are the threshold in a grain and the additional energy that exists on GBs, respectively. **Figure 2(b)** shows the distribution of U_s in grains and GBs. Most GBs are high-angle GBs (red lines), which are much weaker than grains (blue media). A few GBs are low-angle GBs (green, yellow, and brown lines), which have various thresholds according to their relative angles.

Voids are set by removing portions of the model particles (**Figure 2(c)**). In the model, the balance distance between nearest neighbor particles is 1 μm, characteristic size of the grains is 10 μm, and the diameter of a round void is 50 μm. The length of the model along the shock direction is 1.6 mm. The model is illustrated schematically in **Figure 3**. A piston composed of two columns of particles is set on the left-hand side of the model; it moves with piston velocity (v_p) towards the right and produces a shock wave, which propagates from the left to the right. In order to reduce computational cost, periodic boundary conditions are applied on the upper and lower boundaries. Free boundary condition has been applied on the right side. At appointed simulation steps, evolution information such as particles' coordinates, velocities, stresses, springs' forces and connection states will be recorded.

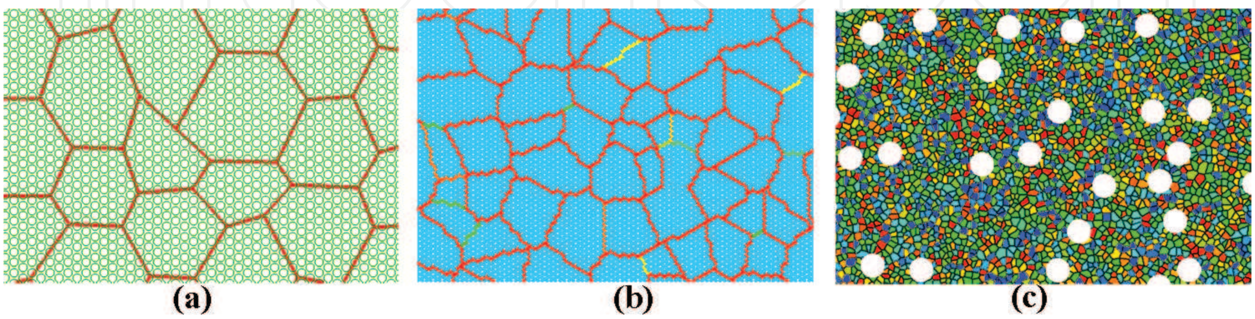

Figure 2. (a) Sketch of polycrystalline model. (b) Fracture energy set in the polycrystalline model. (c) Sketch of porous ceramics. White circles are randomly distributed voids and small colored dots are grains.

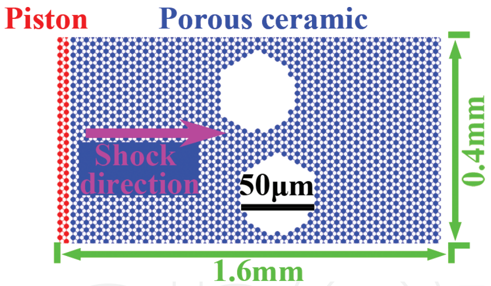

Figure 3. Schematic of the shock wave compression model for porous ceramics.

3. Mechanisms of damage and deformation in shocked porous ceramics

A shock wave relates to a high-power pulse, in which stress and the energy are sufficient to vanquish toughness of ceramics. It would activate pre-existing defects (e.g., microvoids, cracks, and grain boundaries), extends cracks, and breaks media. Mechanical, electrical, and optical properties of ceramics are severely affected by shock waves [28–30], and consequently, it may deteriorate the designed functions of ceramics. Hence, revealing the mechanisms of damage and deformation in shocked porous ceramics would be a foundation for modulation of shock behavior and enhancement of robustness of the porous ceramics involving shock applications. In this section, the effects of voids and grain boundaries on the mesoscopic deformation features of shocked porous ceramics have been explored and compared with shock experiments with the recovery of shocked porous ceramics. Microscope photographs of voids in the recovered sample have been analyzed and compared with computational results. A novel mechanism of slippage and rotation deformation has been revealed, which contributes to and enhances inelastic deformation of the shocked brittle materials. As the pressure increases, the rotational deformation becomes a universal and important mechanism for relieving shear stress and dissipating strain energy.

3.1. Void collapse under shock wave compression

Simulations reveal that void collapse is initiated from severe shear stress concentrations around the void after the shock sweeps through. When media far from the void experience a mild shear stress, media in four corners around the void achieve the fracture criterion. **Figure 4** shows an isolated void that swept by a shock wave. Four shear cracks extend from the void, and broken fragments fill into void along shear cracks and occupy the free volume.

To validate the computational results, shock experiments with the recovery of shocked porous ceramics have been implemented [31]. The lead zirconate titanate (PZT) ceramic has been used, which is a ferroelectric ceramic and generates megawatts of electrical power in a short period of time via a ferroelectric-to-antiferroelectric phase transformation driven by the shock wave from a high-explosive. Unpoled samples have been used, which have no bound charge and charge releasing under the shock experiments. Voids in the ceramics were introduced during fabrication by adding spherical polymethyl methacrylate particles. As shown in **Figure 5(a)**,

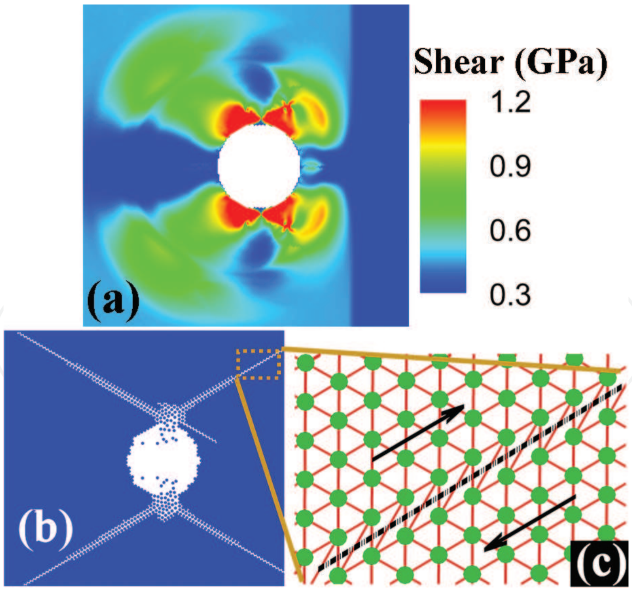

Figure 4. Mesoscopic mechanisms of shock plasticity in porous brittle material. (a) Distribution of the maximum resolved shear stress when shock wave has just swept through a void. (b) A snapshot of shear cracks extension around the void after shock wave has swept through. (c) Relative slippage and rotational deformation revealed in post-shocked region.

the voids in sintered ceramics have diameters of ~50 μm. Bulk density of the samples is determined using the Archimedes method, and the sample porosity is calculated from the ratio of the bulk density to the theoretical density (ρ_0 = 8010 kg/m^3). The sample porosity is 9.3%.

In the recovery experiment, one wants to recover porous ceramic that contains shock compression fracture, and this fracture should only be produced by high-speed impact between the flyer and the target. Therefore, a momentum trap (**Figure 5(b)**), which has the same shock impedance as the ceramic, is needed to bear the intense dynamic tension produced by rarefaction waves and to fly away alone carrying most of the momentum input by the flyer. **Figure 5(c)** shows an incised sample: an integral recovered ceramic (yellow) is conserved in a brown brass packet. Samples are polished and acid etched before scanning electron microscopy (SEM) studies.

Figure 6 shows comparison of void collapse features observed in the model with an isolated void and recovered porous ceramics. Long-distance extended cracks that are emitted from voids are an important feature in the model (**Figure 6(a)**). **Figure 6(b)** shows representative

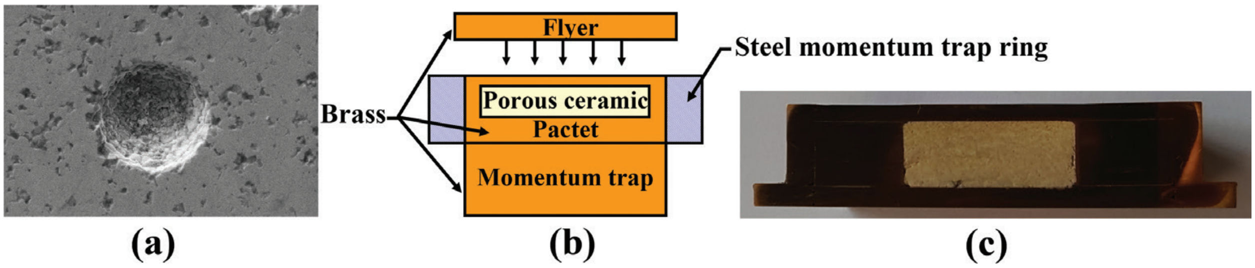

Figure 5. (a) Microscopic observation of a void in initial porous lead zirconate titanate ceramic. (b) A schematic of the shock experiment with recovery of the shocked porous ceramics. (c) Cross section of a recovered sample.

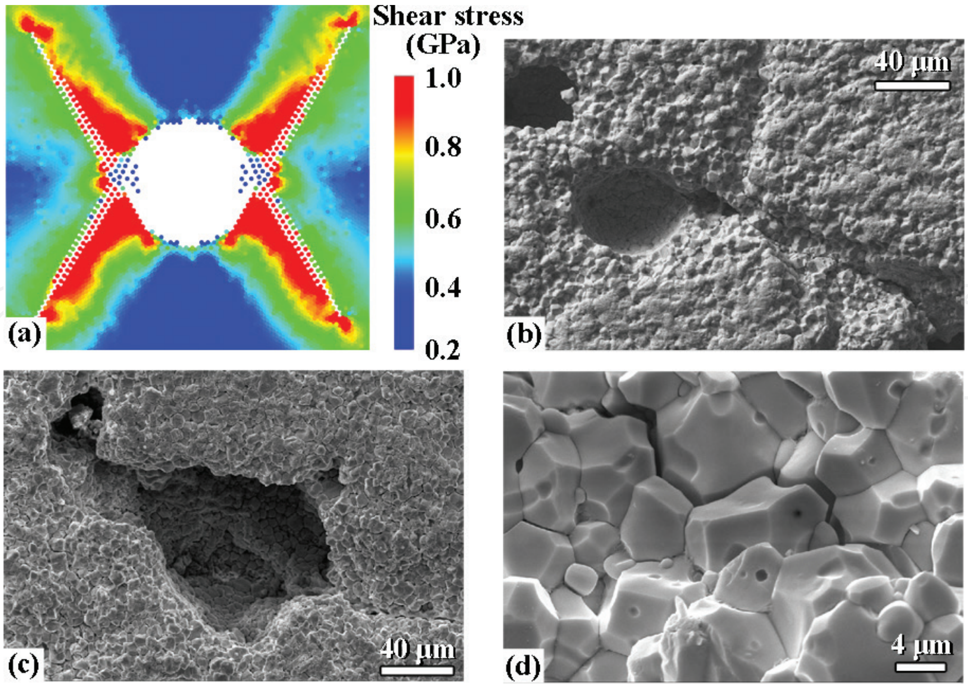

Figure 6. (a) Shear cracks emit from the void because of shear stress concentrations after the exposure to a shock wave. (b) Long-distance extended cracks and (c) thick cranny are observed representative mesoscopic deformation features. (d) Minor crack advances along GBs.

long cracks in the recovery sample subjected to 3.3 GPa compression. The extended crack directions deviate from those around the modeled isolated void (**Figure 6(a)**), and only two cracks are emitted. In **Figure 6(c)**, no long crack exists around this void; instead, a thick crevice forms at the top left corner of the void. It can be deduced that numerous grains in this area were damaged by multicracks and were scaled off during polishing to form such a feature. Many cracks that advance along GBs of porous PZT ceramic have been observed (**Figure 6(d)**). Hence, a more complex model, including multivoid and GBs, would be needed to reproduce these damaged features.

3.2. Characters of shear cracks around collapsing voids

Features of void collapse and shear fracture obtained from the polycrystalline model containing multivoid have been analyzed. In **Figure 7(a)**, fragments of grains fill a damaged void, and long shear cracks extend from the void. All fragments have been removed in **Figure 7(b)** to compare with experimental observations (**Figure 7(c)**). In **Figure 7(d)**, a wide area on the bottom left corner of the void has been damaged during crack evolution. When all fragments have been removed, a thick crevice is visible (**Figure 7(e)**), which is comparable with the deformation feature observed experimentally (**Figure 7(f)**). **Figure 7(g–i)** compares damage features between two voids. A few minor cracks, which are similar to the intergranular crack in **Figure 6(d)**, exist around all the voids in the polycrystalline model.

The polycrystalline model also reveals the evolution of long cracks and thick crevices. For long cracks, an initially transgranular crack translates into an intergranular cracks after a certain propagation range. The translation should occur when the crack-driving force is decreased to a

http://dx.doi.org/10.5772/intechopen.72246

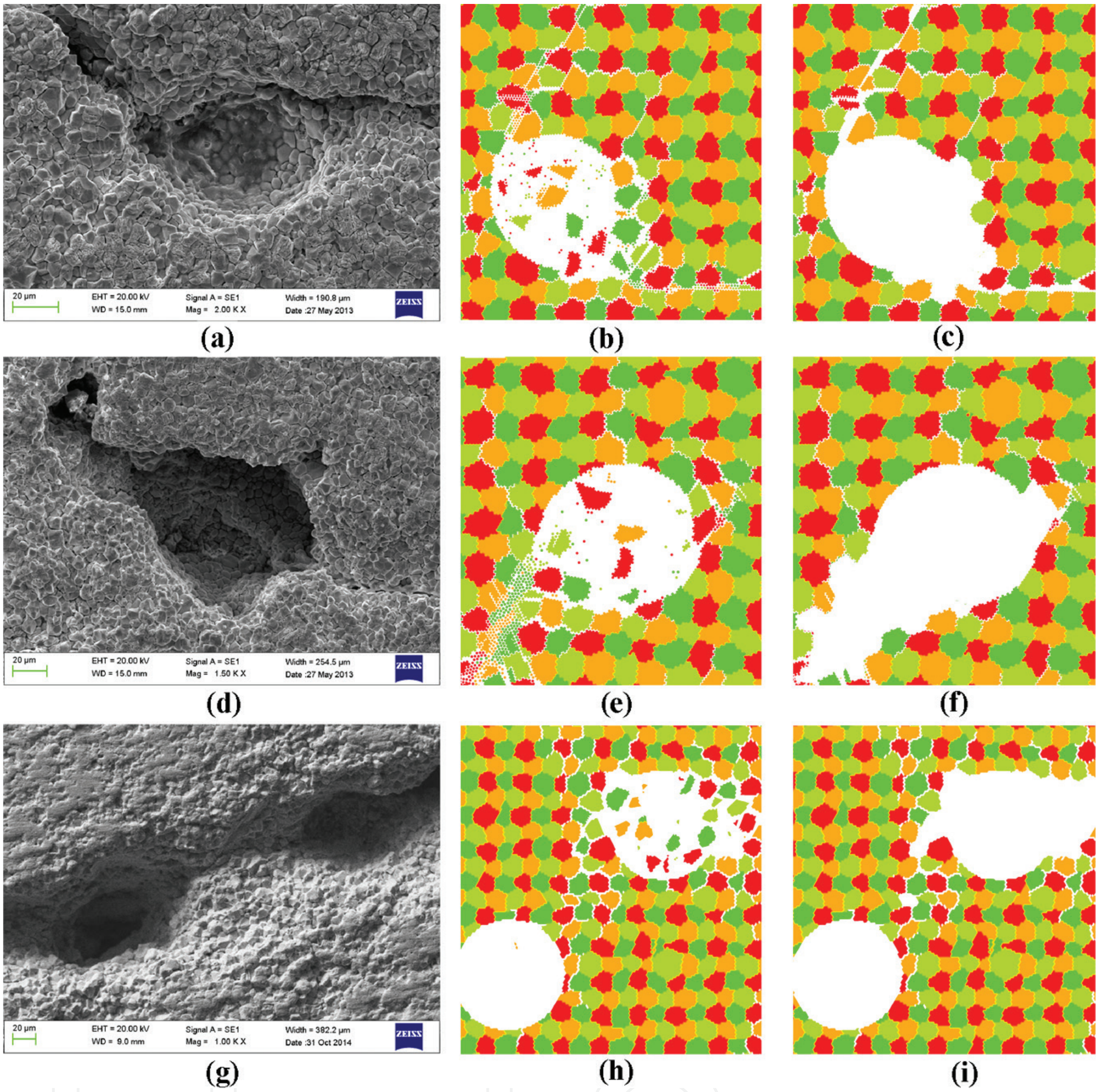

Figure 7. Comparison of deformation features observed in the polycrystalline model and recovery sample. (a)–(c) Representative long-distance extended shear cracks. (d)–(f) Representative thick crevices. (g)–(i) Crack transfixion between two voids.

value that cannot support transgranular fractures. This fracture mode is termed "transgranular-to-intergranular crack mode." However, intergranular cracks branch from the main transgranular crack during main crack propagation to form thick crevices. This fracture mode is termed "main (transgranular) crack and branching (intergranular) cracks mode." Media in a wide area will be damaged in this fracture mode, and a thick crevice becomes visible after fragments have been removed.

What is the dominant factor that leads to these two different fracture modes? As shown in **Figure 7(d)**, the main crack comminutes media in a wide area during its propagation. The thickness of the main transgranular crack is ~10 μm. The violent extension of the main crack implies that the crack-driving force is very strong. The branching of numerous intergranular cracks from the main transgranular crack may be attributed to the need for more effective shock energy dissipation.

3.3. Slippage and rotational deformation of shatters

A novel mechanism of slippage and rotation deformation, which contributes to and enhances inelastic deformation of the shocked brittle materials, has been revealed by this model. In shocked porous ceramic, numerous shear cracks are emitted during void collapse, forming a crack network. As a consequence, the media are comminuted into scattered tiny shatters by interlaced cracks. When the field of the relative velocity in these comminuted regions is drawn (**Figure 8**), the arrows (which indicated the relative velocities and directions of media) revealed complex vortex structures, showing that the shatters were slipping and rotating under shock [17]. The complex vortex structures indicate that the network composed of shear cracks takes a similar role to that of shear bands in high-strength high-toughness metallic glasses [32, 33]. They provide the precondition for relative slippages of media and irreversible deformation of the sample.

The rotational deformations of different types of materials have been reported in shock and static high-pressure investigations carried out by experiments and simulations [34–38]. For example, nickel nanoparticles were found to rotate in a diamond anvil cell when the pressure rose from 3 GPa to more than 38 GPa. When the particle sizes were various from 500 nm down to 3 nm, the measurements indicated that more active grain rotation occurs in the smaller nickel nanocrystals. Investigations here and in literatures about rotational deformation of various materials and loading conditions indicate that it becomes a universal and important deformation mechanism under high pressure to help the loaded systems to relieve shear stress and dissipate strain energy, when other usual deformations (e.g., dislocation, twinning) are absent or repressed [38, 39].

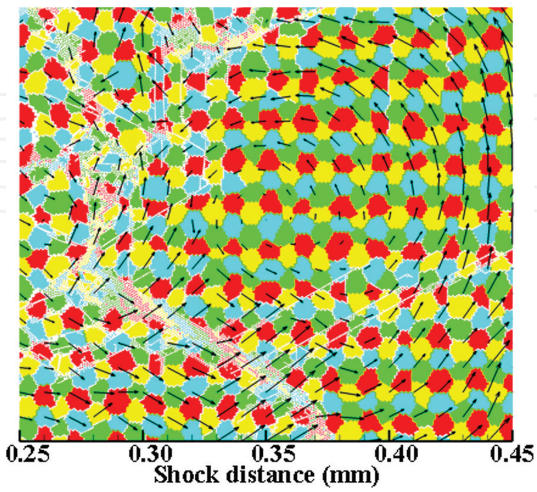

Figure 8. Slippage and rotation of shatters induced by extending shear cracks.

http://dx.doi.org/10.5772/intechopen.72246

4. Design of energy absorbing and fracture control in shocked porous ceramics

Pre-existing defects in ceramics induce shock wave compression fractures and may lead to the failure of designed functions. One traditional strategy for failure prevention has been by sintering "defect-free" ceramics (e.g., a large, perfect single-crystal sample). However, such treatment by sintering is difficult in practice and costly in expense, and more importantly, it only increases the critical emergence stress of shock fracture rather more than eliminating the probability of shock failure. Adopting an approach that is the opposite of creating defect-free ceramics, one may be able to control shock fracture and avoid the shock failure of ceramics by properly introducing defects. The control of shock fracture by introducing defects may seem counterintuitive. However, under quasi-static loading, there have already been many successful cases in which defects are introduced to avoid catastrophic fracture. In nature, highly mineralized natural materials owe their exceptional toughness and quasi-ductility to microscopic building blocks, weak interfaces and architecture [40–42]. In engineering, the fracture toughness of "hard and brittle" glass and metal glasses has been increased by properly introducing microcracks and voids [43–45]. These mechanisms can be summarized as crack shielding, deflection, and bridging, which effectively reduce the crack-driving force [46]. In shock applications, however, the difference is that a shock wave relates to a high-power pulse. The stress and the energy input are sufficient to vanquish various toughening strategies. Hence, numerous cracks nucleate and grow inevitably. In this case, strategies for toughening brittle materials cannot be duplicated. Instead, a novel approach in addressing shock fracture is proposed, i.e., modulating the propagation of crack network in shocked ceramics by deliberately adding pores.

4.1. Control of the fractured region

Mesoscopic damage and deformation evolutions (void collapse, shear fracture, and rotational deformation) induced significant stress relaxation, leading to macroscopic "plastic" response, although the model particles and springs did not contribute to plasticity (only a linear elastic interaction was set in springs of the model). Note that here plasticity is taken in its broadest sense; it is identified not by dislocation movements, but by the macroscopic stress-strain curve and irreversible deformations. **Figure 9** shows the correlation between macroscopic plasticity and mesoscopic damage evolution. Initially, a steep shock front is induced by the impact of the piston. The shock front broadens and splits into two waves during propagation inside a sample. The precursor wave is an elastic wave, which propagates with longitudinal acoustic speed. The second wave, which corresponds to an irreversible deformation, is usually termed the deformation wave (it is called plastic wave in ductile metals). The propagation speed of the deformation wave is slower than the elastic wave; thus, a plateau is produced between these two waves. After the deformation wave, the final equilibrium state, namely the Hugoniot state, is achieved. The deformation wave and the following plateau (the Hugoniot state) correspond to a "severely fractured state (SFS)," where shear fracture, void collapse, and rotational deformation of comminuted media are processed abundantly [10]. Note that the deformation wave and

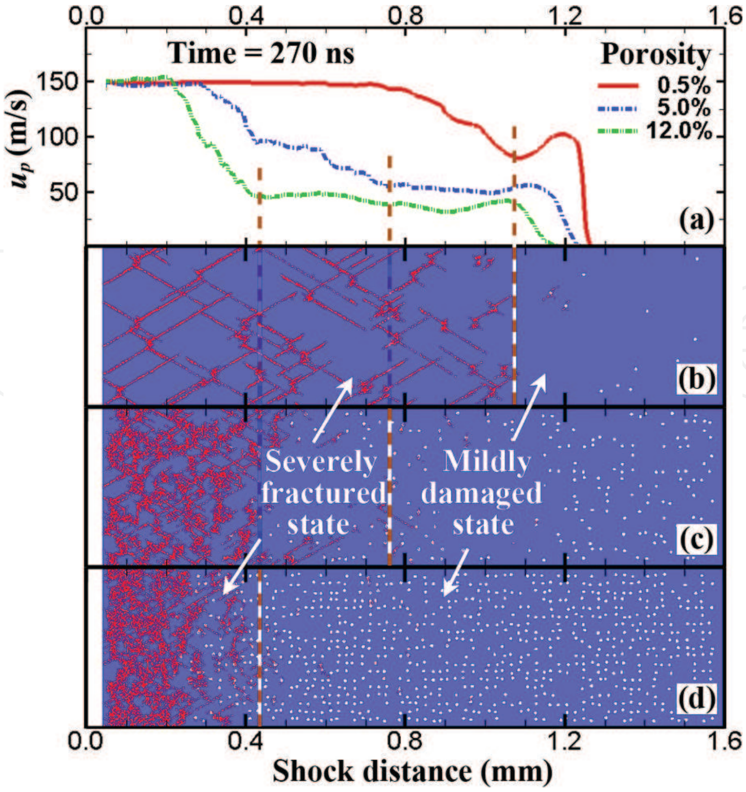

Figure 9. Comparison of (a) shock wave profiles and (b–d) damage distributions in dense, 5, and 12% porous ceramics, respectively.

the SFS propagate synchronously. If the deformation wave is unloaded, then, without enough energy to maintain damage evolution, the SFS would be "frozen." This is the foundation for modulating shock fracture.

Figure 10 shows schematics of controlling shock fracture. A traditional strategy for doing it is sintering "fully dense" ceramics (**Figure 10(a)**). Evolution of a dense sample with only 0.5%

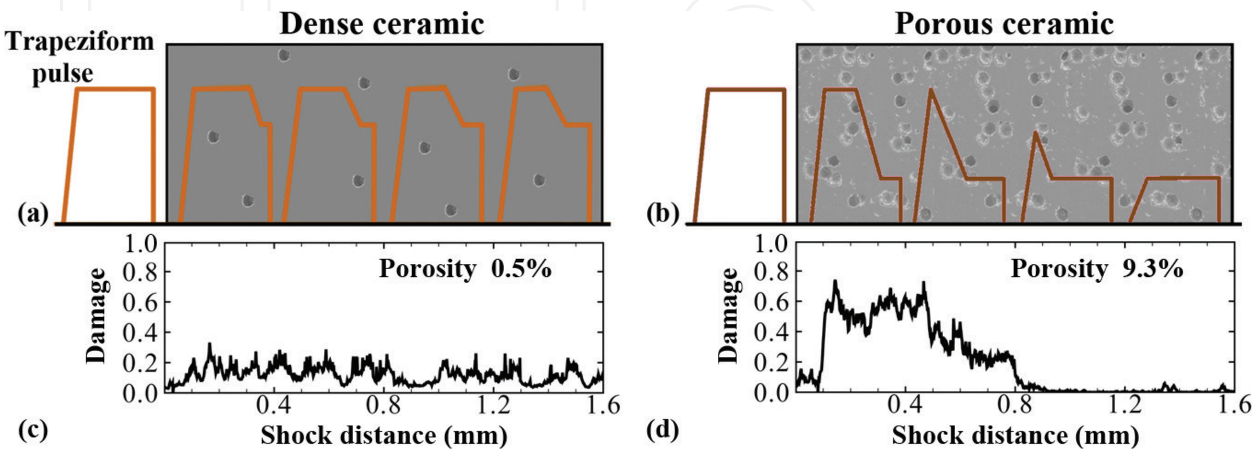

Figure 10. Schematic of short pulse evolutions in (a) dense ceramic (with 0.5% porosity) and (b) porous ceramic (with 9.3% porosity). Degrees of damage of (c) dense and (d) porous samples at 800 ns after impact.

porosity was therefore simulated; **Figure 10(c)** shows that its average degree of damage is reduced to ~0.1, but the damage is distributed throughout the sample. An alternative approach is worth looking for. Instead of sintering fully dense ceramics, a new idea is to make use of the pores. As shown in **Figure 10(b)**, voids are deliberately added in the ceramic; **Figure 10(d)** shows the degree of damage of a porous sample with 9.3% porosity (it is the porosity of PZT ceramics used in experiments) after sufficient evolvement: half of the porous sample has an average damage of ~0.4, and the other half of the sample is almost intact. A "shielded region" is acquired at the cost of severe fracture in the other parts of the sample (the "damaged region").

The design of controlling fractured region is based on the following mechanism: (1) the deformation wave would be slowed down by the deliberately increased porosity; (2) if the pulse is short compared with the thickness of the sample, then a rarefaction wave (the "trailing edge" of a stress pulse of shock) would catch up and unload the slow deformation wave; (3) the SFS would be frozen after the deformation wave vanishes, rather than sweep through the entire sample. After that, the ceramic will undergo elastic compression and stay in a mildly damaged state.

4.2. Validation by LSM simulation

Figure 11(a) shows the configuration of the model to investigate whether voids can protect part of a sample away from the SFS. In one of the simulation runs, the porosity of the sample is 9.3% and the velocity of the flyer v_f=300 m/s, which induces a ~5 GPa shock stress. The ultimate damage distribution after sufficient evolvement is shown in **Figure 11(b)**. Half of the sample is in the SFS, whereas the other half is basically intact. **Figure 11(c)** plots three shock wave profiles at three midterm times. At 130 ns after impact, an elastic wave-deformation wave-rarefaction wave structure has formed; at 240 ns, the rarefaction wave has caught the deformation wave; at 350 ns, the deformation wave has unloaded completely, and the SFS should be frozen at that time. Indeed, the boundary between the damaged region and shielded region at 800 ns in **Figure 11(b)** matches the position where the deformation wave vanished in **Figure 11(c)**.

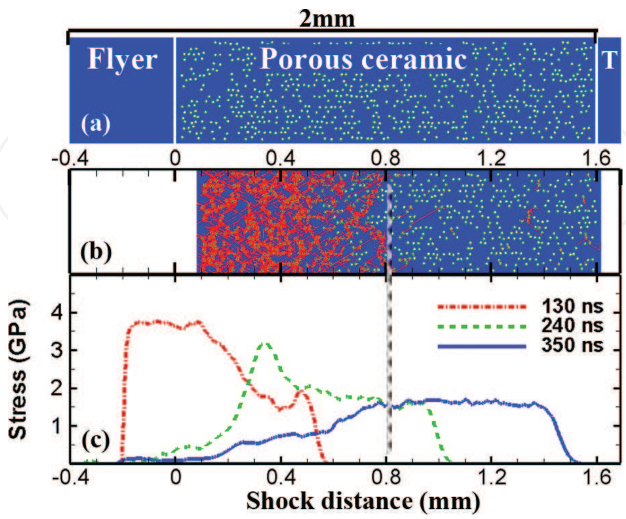

Figure 11. Mechanism of earning a shielded region where the severely fractured state will not enter. (a) Configuration of the model. T refers to a very long momentum trap. (b) Damage distribution in the sample at 800 ns. (c) Stress wave evolution at three midterm times.

Damage evolutions of dense, 5, and 12% porous ceramics have been further simulated and their ultimate damage distributions after the flyer impact at 300 m/s are compared. **Figure 12** plots the void collapse ratio $r_{collapse}$ for all samples. The samples are divided into segments; the $r_{collapse}$ is calculated from the ratio of the number of collapsed voids to the total number of voids in each segment. The boundary between the damaged region and shielded region corresponds to a rise of $r_{collapse}$ from 0 to 1. For the same shock stress and the pulse width, as the porosity increases, the thickness of the shielded region increases accordingly. The dense ceramic has no shielded region, whereas the 12% porous ceramic has a shielded region of about 1 mm.

4.3. Validation by soft recovery experiment

Figure 13(a) and **(e)** shows the fracture characteristics of the sample subjected to a compression of 3.3 GPa and that of 1.4 GPa, respectively. Each image is composed of 19 SEM frames, which are successively scanned along the "scanned area" marked in **Figure 13(b)**. The image has a width of 766 μm and a length of nearly 8 mm. The direction of the shock wave propagation is from the left of the image to the right. The green circles represent the voids that are basically intact. **Figure 13(c)** shows that they are concavities that are almost hemispheric and show no sign of collapse. The red rectangles represent the voids that have collapsed. **Figure 13(d)** shows that they are hollows that are believed to have been voids, but no longer retains their hemispheric shape.

For the sample loaded by a 3.3 GPa shock wave, an elastic wave-deformation wave structure emerged once, then the deformation wave is unloaded. The shield ratio should be r^{shield}≈0.76, which means that ~1/4 of the sample would stay in the SFS and the other ~3/4 of the sample would be shielded. In **Figure 13(a)**, all the voids close to the impact surface have collapsed; but in the other half of the sample, there are numerous voids that are basically intact. While the distribution of the collapsed voids in the experimental samples is not as ideal as that in the modeled sample, this sample can still be divided distinctly into a damaged region and a shielded one. However, for a fully dense (0.5%-porous) sample, the simulation showed that a shielded region did not form under the same condition. For the sample loaded by a 1.4 GPa shock wave, only one elastic wave (which would not cause void collapse) emerged. And in **Figure 13(e)**, basically intact voids can be found throughout the sample.

The results obtained from simulations and experiments have a similar trend, except that about 40% of the voids were identified as collapsed void in the shielded region of the experimental

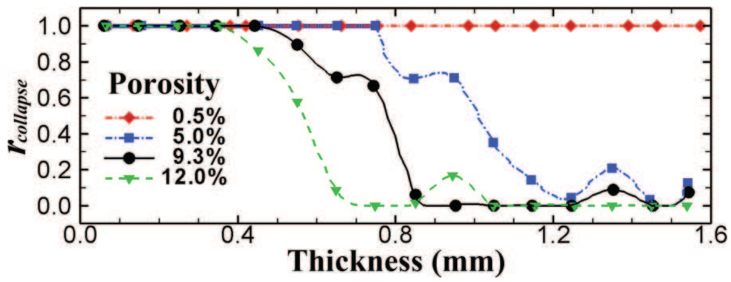

Figure 12. Comparison of collapse ratios of dense and porous samples with different porosities under the same shock stress and pulse width. $r_{collapse}$ represents collapse ratio.

http://dx.doi.org/10.5772/intechopen.72246

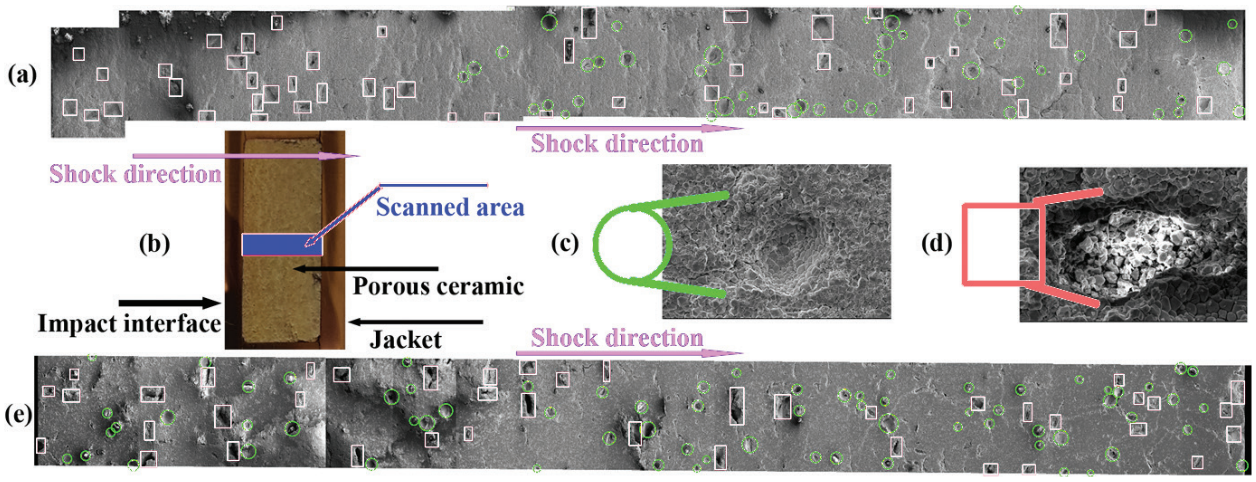

Figure 13. Fracture character of porous ceramics in recovery experiments. (a) Voids evolution in the sample subjected to compression of 3.3 GPa. (b) Cross section of recovery sample. (c) Green circle represents basically intact void. (d) Red rectangle represents void which has collapsed. (e) Voids evolution in the sample subjected to compression of 1.4 GPa.

sample. We attribute this "additional damage" in the shielded region of the recovered sample to two main reasons. First, there is roughness on the rear interface between the ceramic and the packet, which induced dynamic tensile stress after the shock wave has swept through and resulted in additional void damage. Second, the PZT ceramic is soft; a lot of grains are scaled off during polishing, which has a significant influence on the results counting. If one deducts the additional damage, then the experimental result is in good agreement with the simulation result.

5. Conclusion

With the lattice-spring model simulation and the shock recovery experiment, mechanisms of damage evolution, including void collapse, shear fracture, and rotational deformation, are illuminated, and their contributions to the damage toleration of the shocked porous ceramics are demonstrated, which would be beneficial to the understanding of porous ceramics in application upon shock wave loading.

Here, adding pores deliberately does not mean to fabricate "foam ceramic." As the porosity increases, the length of the shielded region increases accordingly, and it should be considered integrally when one designs porous ceramics.

Author details

Yin Yu and Hongliang He*

*Address all correspondence to: honglianghe@caep.cn

National Key Laboratory of Shock Wave and Detonation Physics, Institute of Fluid Physics, CAEP, Mianyang, Sichuan, People's Republic of China

References

[1] Kanel GI, Zaretsky EB, Rajendran AM, Razorenov SV, Savinykh AS, Paris V. Search for conditions of compressive fracture of hard brittle ceramics at impact loading. International Journal of Plasticity. 2009;**25**:649-670. DOI: https://doi.org/10.1016/j.ijplas.2008.12.004

[2] Grady DE. Shock-wave compression of brittle solids. Mechanics of Materials. 1998;**29**: 181-203. DOI: https://doi.org/10.1016/S0167-6636(98)00015-5

[3] Bourne NK, Millett JCF, Rosenberg Z, Murray N. On the shock induced failure of brittle solids. Journal of the Mechanics and Physics of Solids. 1998;**46**:1887-1908. DOI: https://doi.org/10.1016/S0022-5096(98)00046-5

[4] Graham RA. Shock-induced electrical activity in polymeric solids. A mechanically induced bond scission model. Journal of Physical Chemistry A. 1979;**83**:3048-3056. DOI: 10.1021/j100486a024

[5] Lankford J, Predebon WW, Staehler JM, Subhash G, Pletka BJ, Anderson CE. The role of plasticity as a limiting factor in the compressive failure of high strength ceramics. Mechanics of Materials. 1998;**29**:205-218. DOI: https://doi.org/10.1016/S0167-6636(98)00023-4

[6] Jiang D, Zhang N, Feng Y, Du J, Gu Y. Electric response of $Pb_{0.99}[(Zr_{0.90}Sn_{0.10})_{0.968}Ti_{0.032}]_{0.98}Nb_{0.02}O_3$ ceramics to the shock-wave-induced ferroelectric-to-antiferroelectric phase transition. Materials Science and Engineering B. 2012;**177**:210-216. DOI: https://doi.org/10.1016/j.mseb.2011.12.015

[7] Zeng T, Dong X, Mao C, Zhou Z, Yang H. Effects of pore shape and porosity on the properties of porous PZT 95/5 ceramics. Journal of the European Ceramic Society 2007; **27**: 2025-2029. DOI: http://dx.doi.org/10.1063/1.3525056

[8] Graham RA, Ingram GE. Piezoelectric current from x-cut quartz subjected to short-duration shock-wave loading. Journal of Applied Physics 1972;**43**:826-835. DOI: http://dx.doi.org/10.1063/1.1661289

[9] Li J, Zhou X, Li J. A time-resolved single-pass technique for measuring optical absorption coefficients of window materials under 100 GPa shock pressures. The Review of Scientific Instruments 2008;**79**:123107-123101-6. DOI: http://dx.doi.org/10.1063/1.3046279

[10] Espinosa HD, Zavattieri PD. A grain level model for the study of failure initiation and evolution in polycrystalline brittle materials. Part I: Theory and numerical implementation. Mechanics of Materials. 2003;**35**:333-364. DOI: https://doi.org/10.1016/S0167-6636(02)00285-5

[11] Espinosa HD, Zavattieri PD. A grain level model for the study of failure initiation and evolution in polycrystalline brittle materials. Part II: Numerical examples. Mechanics of Materials. 2003;**35**:365-394. DOI: https://doi.org/10.1016/S0167-6636(02)00287-9

[12] Zavattieri PD, Raghuram PV, Espinosa HD. A computational model of ceramic microstructures subjected to multi-axial dynamic loading. Journal of the Mechanics and Physics of Solids. 2001;**49**:27-68. DOI: https://doi.org/10.1016/S0022-5096(00)00028-4

[13] Silling SA. Reformulation of elasticity theory for discontinuities and long-range forces. Journal of the Mechanics and Physics of Solids. 2000;**48**:175-209. DOI: https://doi.org/10.1016/S0022-5096(99)00029-0

[14] Case S, Horie Y. Discrete element simulation of shock wave propagation in polycrystalline copper. Journal of the Mechanics and Physics of Solids. 2007;**55**:589-614. DOI: https://doi.org/10.1016/j.jmps.2006.08.003

[15] Wang YC, Mora P. Modeling wing crack extension: Implications for the ingredients of discrete element model. Pure and Applied Geophysics. 2008;**165**:609-620. DOI: https://doi.org/10.1007/978-3-7643-8757-0_9

[16] Buxton GA, Care CM, Cleaver DJA. lattice spring model of heterogeneous materials with plasticity. Modelling Simul. Materials Science and Engineering. 2001;**9**:485-497. DOI: http://iopscience.iop.org/article/10.1088/0965-0393/9/6/302/meta

[17] Yu Y, Wang W, He H, Lu T. Modeling multiscale evolution of numerous voids in shocked brittle material. Physical Review E. 2014;**89**:043309-1-8. DOI: https://doi.org/10.1103/PhysRevE.89.043309

[18] Cundall PA. A discrete numerical model for granular assemblies. Geotechnique. 1979;**1**:47-65. DOI: http://www.icevirtuallibrary.com/doi/pdf/10.1680/ege.35362.0025

[19] Alava MJ, Nukala PKVV, Zapperi S. Statistical models of fracture. Advances in Physics 2006;**55**:349-476. DOI: http://dx.doi.org/10.1080/00018730300741518

[20] Pazdniakou A, Adler PM. Lattice spring modles. Transport in Porous Media. 2012;**93**:243-262. DOI: 10.1007/s11242-012-9955-6

[21] Griffith AA. The phenomena of rupture and flow in solids. Philosophical Transactions of the Royal Society of London. 1920;**221**:163-198. DOI: http://www.jstor.org/stable/91192

[22] Zhao GF, Fang JN, Zhao J. A 3D distinct lattice spring model for elasticity and dynamic failure. International Journal for Numerical and Analytical Methods in Geomechanics. 2011;**35**:859-885. DOI: 10.1002/nag.930

[23] Ostoja-Starzewski M. Lattice models in micromechanics. Applied Mechanics Reviews. 2002;**55**:1-26. DOI: 10.1115/1.1432990

[24] Grah M, Alzebdeh K, Sheng PY, Vaudin MD, Bowman KJ, Ostoja-Starzewski M. Brittle intergranular failure in 2D microstructures: Experiments and computer simulations. Acta Materialia. 1996;**44**:4003-4018. DOI: https://doi.org/10.1016/S1359-6454(96)00044-4

[25] Wang Y, Yin XC, Ke FJ, Xia MF, Peng KY. Numerical simulation of rock failure and earthquake process on mesoscopic scale. Pure and Applied Geophysics. 2000;**157**:1905-1928. DOI: https://doi.org/10.1007/PL00001067

[26] Gusev AA. Finite element mapping for spring network representations of the mechanics of solids. Physical Review Letters. 2004;**93**:034302-1-4. DOI: https://doi.org/10.1103/PhysRevLett.93.034302

[27] Walsh JB. The effect of cracks on the compressibility of rock. Journal of Geophysical Research. 1965;**70**:381-389. DOI: 10.1029/JZ070i002p00381

[28] Chen MW, McCauley JW, Dandekar DP, Bourne NK. Dynamic plasticity and failure of high-purity alumina under shock loading. Nature Materials. 2006;**5**:614-618. DOI: 10.1038/nmat1689

[29] Zhang F, He H, Liu G, Liu Y, Yu Y, Wang Y. Failure behavior of Pb(Zr0.95Ti0.05)O3 ferroelectric ceramics under shock compression. Journal of Applied Physics. 2013;**113**:183501-1-7. DOI: https://doi.org/http://dx.doi.org/10.1063/1.4803052"http://dx.doi.org/10.1063/1.4803052

[30] Hao GY, Liu FS, Zhang DY, Zhang MJ. Optical emission of directly contacted copper/sapphire interface under shock compression of megabar. Applied Physics Letters. 2007;**90**:261914-1-3. DOI: http://dx.doi.org/10.1063/1.2751606

[31] Yu Y, Wang WQ, He HL, Jiang TL, Huan Q, Zhang FP, Li YQ, Lu TC. Mesoscopic deformation features of shocked porous ceramic: Polycrystalline modeling and experimental observations. Journal of Applied Physics. 2015;**117**:125901-1-8. DOI: http://dx.doi.org/10.1063/1.4916244

[32] Hofmann DC, Suh JY, Wiest A, Lind ML, Demetriou MD, Johnson WL. Development of tough, low-density titanium-based bulk metallic glass matrix composites with tensile. Nature. 2008;**451**:1085. DOI: 10.1073/pnas.0809000106

[33] Chen LY, Fu ZD, Zhang GQ, Hao XP, Jiang QK, Wang XD, Cao QP, Franz H, Liu YG, Xie HS, Zhang SL, Wang BY, Zeng YW, Jiang JZ. Physical Review Letters. 2008;**100**:075501. DOI: https://doi.org/10.1103/PhysRevLett.100.075501

[34] Yano K, Horie Y. Discrete-element modeling of shock compression of polycrystalline copper. Physical Review B. 1999;**59**:13672-13680. DOI: https://doi.org/10.1103/PhysRevB.59.13672

[35] Mescheryakov YI, Mahutov NA, Atroshenko SA. Micromechanisms of dynamic fracture of ductile high-strength steel. Journal of the Mechanics and Physics of Solids. 1994;**42**:1435-1457. DOI: https://doi.org/10.1016/0022-5096(94)90004-3

[36] Chen B, Lutker K, Lei J, Yan J, Yang S, H-k M. Detecting grain rotation at the nanoscale. Proceedings of the National Academy of Sciences of the United States of America. 2014;**111**:3350-3353. DOI: 10.1073/pnas.1324184111

[37] Ma W, Zhu W, Jing F. The shock-front structure of nanocrystalline aluminum. Applied Physics Letters 2010; **97**: 121903-121901-3. DOI: http://dx.doi.org/10.1063/1.3490643

[38] Schiøtz J, Jacobsen KW. A maximum in the strength of nanocrystalline copper. Science. 2003;**301**:1357-1359. DOI: 10.1126/science.1086636

[39] FDi G, JQ-da F. An experimental study of the polycrystalline plasticity of austenitic stainless steel. International Journal of Plasticity. 2015;**74**:92-109. DOI: https://doi.org/10.1016/j.ijplas.2015.05.012

[40] Yahyazadehfar M, Bajaj D, Arola DD. Hidden contributions of the enamel rods on the fracture resistance of human teeth. Acta Biomaterialia. 2013;**9**:4806-4814. DOI: https://doi.org/10.1016/j.actbio.2012.09.020

[41] Barthelat F, Rabiei R. Toughness amplification in natural composites. Journal of the Mechanics and Physics of Solids. 2011;**59**:829-840. DOI: https://doi.org/10.1016/j.jmps.2011.01.001

[42] Barthelat F, Tang H, Zavattieri PD, Li CM, Espinosa HD. On the mechanics of mother-of-pearl: A key feature in the material hierarchical structure. Journal of the Mechanics and Physics of Solids. 2007;**55**:306-337. DOI: https://doi.org/10.1016/j.jmps.2006.07.007

[43] Mirkhalaf M, Dastjerdi AK, Barthelat F. Overcoming the brittleness of glass through bio-inspiration and micro-architecture. Nature Communications. 2014;**5**:3166-1-9. DOI: 10.1038/ncomms4166

[44] Sarac B, Schroers J. Designing tensile ductility in metallic glasses. Nature Communications. 2013;**4**:3158-1-7. DOI: 10.1038/ncomms3158

[45] RT Q, Zhao JX, Stoica M, Eckert J, Zhang ZF. Macroscopic tensile plasticity of bulk metallic glass through designed artificial defects. Materials Science and Engineering A. 2012;**534**:365-373. DOI: https://doi.org/10.1016/j.msea.2011.11.082

[46] Launey ME, Ritchie RO. On the fracture toughness of advanced materials. Advanced Materials. 2009;**21**:2103-2110. DOI: 10.1002/adma.200803322